Multibistability and self-pulsation in nonlinear high-Q silicon microring resonators considering thermo-optical effect

Libin Zhang, Yonghao Fei, Tongtong Cao, Yanmei Cao, Qingyang Xu, and Shaowu Chen[*]

State Key Laboratory on Integrated Optoelectronics, Institute of Semiconductors, Chinese Academy of Sciences, Beijing 100083, China
(Received 30 November 2012; published 6 May 2013)

Optical bistability (BI) and self-pulsation (SP) in high-Q silicon microring resonators (MRRs) induced by thermo-optical (TO) effect and other nonlinear effects are theoretically studied with coupled mode theory and linear stability analysis method. It is found that the boundaries for both BI and SP are mainly restricted by two counteracting effects: free carrier dispersion effect and TO effect. If the refractive index changes of a MRR caused by these two effects are on the same order of magnitude, the output power will exhibit much more complicated dependence on the input power and wavelength, namely, input-power-dependent multi-BI and multi-SP regions will exist at certain input wavelength range. The controllability of multi-BI and multi-SP phenomena by the input power and input wavelength could be very useful in all-optical nonlinear devices.

I. INTRODUCTION

Silicon microring resonators (MRRs) have shown great potential in passive and active photonic devices. With the decrease of the cross section as well as the linear loss for the ring waveguide, the threshold power for the onset of bistability (BI) and self-pulsation (SP) can be effectively lowered. Currently, linear loss of silicon MRRs has been reduced to less than 0.8 dB/cm by using the etchless technology, resulting in an intrinsic quality factor higher than 510 000 [1]. Meanwhile, the waveguide geometric dimension has been reduced from several micrometers to several hundred nanometers, immensely enhancing the light intensity within the ring waveguide. The minimum threshold power has been reported as 277 μW (BI) [2] and 300 μW (SP) [3] for etched SOI resonators and 42 μW (BI) for etchless silicon MRRs [4], respectively. Besides MRRs, other types of silicon resonators have been employed to further reduce the threshold power as well, with 35 μW (BI) and 480 μW (SP) for silicon microdisk resonators [5] and 25 μW (BI) for silicon photonic crystal nanocavities [6]. The lower threshold power of BI and SP is useful in all-optical modulation and logic devices. However, such low threshold power may have a negative influence on the functions of some passive devices based on silicon resonators, for example, optical routers and splitters, as a slightly higher input power (about 0.1 mW) would arouse undesired disturbance on their normal functionalities.

SP can occur in passive ring cavities when the relaxation time of the nonlinear medium is much longer than the round-trip time of the ring, which is proposed by Ikeda [7]. In silicon MRR, such relaxation time includes photon lifetime, free carrier lifetime and thermal decay time. S. Malaguti *et al.* [8] and we [9] both analyzed the BI and SP phenomena without considering the thermo-optical (TO) effect. Several articles have reported thermo-induced BI and SP in silicon resonators previously [3,5]. However, it is not yet clear how the associated parameters affect the dynamic behaviors of these nonlinear phenomena. Recently, Van Vaerenbergh, *et al.* [10,11] have analyzed the TO effect on the nonlinear behavior of silicon

MRRs, but they neglected the fast light dynamics, i.e., the photon lifetime in silicon MRRs.

In this paper, we have investigated the individual effect of the three time constants on the regions of BI and SP, with emphasis on the effect of the free carrier lifetime and the thermal decay time. An interesting result is found that if we choose proper free carrier lifetime and thermal decay time, we will get multi-BI and multi-SP when changing input power, which has not been reported yet. A further study on different SP regions shows that the oscillation frequencies and output power waveforms are much different. The effects considered in our model include linear loss, linear absorption, two-photon absorption (TPA), TPA-induced free carrier absorption (FCA) and FCD, Kerr nonlinearity, and TO effect [12,13]. Free carriers generated by TPA play a twofold role in terms of refractive index change: first, they decrease the refractive index of the waveguide by the FCD effect; second, the interband and intraband relaxation of these free carriers induces phonon excitation, which raises the temperature in the waveguide through lattice vibration, and in turn increases the refractive index due to TO effect. As a result of the different response time of these two opposite effects, the output power of the MRR becomes much more complicated with respect to varying input power and wavelength.

The article is organized as follows. The model is introduced in Sec. II including TO effect and other physical effects. We then normalize these equations and give the linear stability analysis. In Sec. III, we analyze BI and SP phenomena using linear stability method. The boundaries for both BI and SP in input power and wavelength are obtained. And the characteristics in different SP regions are studied in time domain and frequency domain. Then we study the effects of free carrier lifetime, thermal decay time, and photon lifetime on the BI and SP. Finally, we conclude the paper.

II. MATHEMATICAL MODEL

A. Nonlinear coupled mode theory

Nonlinear coupled mode theory (CMT) is used to describe the light propagation in silicon MRRs. Similar to those described in [14–17], the temporal evolution of the intracavity

---

[*]swchen@semi.ac.cn

053805-1

field $u(t)$ can be described as follows:

$$\frac{\partial u}{\partial t} = \left\{ -i\frac{\omega_L}{n_0}\left[\frac{n_2 c}{n_0 V_{Kerr}}|u|^2 - (\sigma_{r1}N + \sigma_{r2}N^{0.8}) + \kappa_\theta \Delta T\right] \right.$$
$$\left. + i(\omega_0 - \omega_L) - \left[\frac{c\alpha}{2n_0} + \frac{\beta_2 c^2}{2n_0^2}\frac{|u|^2}{V_{TPA}} + \frac{\sigma_{FCA}Nc}{2n_0}\right]\right\} u$$
$$+ \sqrt{\Gamma_c P_{in}}, \tag{1}$$

where c is the light velocity in vacuum, u is the complex amplitude of light propagating in the MRR by letting $|u|^2$ equal to the mode energy $U = |u|^2$, n_0 is the refractive index of the MRR, ω_0 is the resonance frequency of the MRR, ω_L is the incident light frequency, and P_{in} is the incident light power. $n_2 c|u|^2/(n_0 V_{Kerr})$ is the refractive index change caused by Kerr effect, with n_2 the Kerr coefficient and V_{Kerr} the Kerr nonlinear volume $V_{Kerr} = A_{Kerr}L$. $-(\sigma_{r1}N + \sigma_{r2}N^{0.8})$ is the refractive index change induced by FCD effect with $\sigma_{r1} = 8.8 \times 10^{-22}$, $\sigma_{r2} = 8.5 \times 10^{-18}$ and electron-hole density N in cm^{-3} [18]. $\kappa_\theta \Delta T$ is the refractive index change induced by TO effect, with κ_θ the TO coefficient $\kappa_\theta = \partial n/\partial T$ and ΔT the temperature change in the ring waveguide. α is the total linear loss of the MRR, including ring linear loss α_{ring} and coupling loss α_c. $\beta_2 c^2|u|^2/(2n_0^2 V_{TPA})$ represents the absorption loss caused by TPA, with β_2 the TPA coefficient and V_{TPA} the TPA volume $V_{TPA} = A_{TPA}L$. $\sigma_{FCA}Nc/(2n_0)$ is the FCA loss, with σ_{FCA} the FCA coefficient. Γ_c is the coupling coefficient between straight waveguide and ring waveguide with $\Gamma_c = c\alpha_c/n_0$.

Under critical coupling conditions, the total microring loss equals to the coupling loss ($\alpha_{ring} = \alpha_c$). $\alpha_{ring} \equiv \alpha_{abs} + \alpha_{rad} + \alpha_{sca}$ means that the ring loss has three parts, i.e. the linear absorption loss α_{abs}, the radiation loss of the higher order mode α_{rad}, and the sidewall roughness scattering loss α_{sca}. The linear absorption involves the material absorption and the surface state absorption. It is generally difficult to determine the exact proportion of linear absorption loss in the ring loss ($\eta_{lin} = \alpha_{abs}/\alpha_{ring}$), and as an example, we assume this proportion to be 0.4, which means that 40% of the ring loss is due to the linear absorption, which would eventually converted to heat to raise the temperature of the waveguide.

Due to the intrinsic connection between TPA and Kerr effects, the effective cross section of TPA effect, denoted by A_{TPA}, equals to that of Kerr effect, denoted by A_{Kerr}, and is defined as $A_{TPA} = \frac{[\iint n(x,y)^2|\mathbf{E}|^2 dxdy]^2}{\iint_{Si} n(x,y)^4|\mathbf{E}|^4 dxdy}$ [5,19].

Free carriers in the ring waveguide are mostly generated by TPA effect. The relaxation of these free carriers involves in a variety of processes, including nonradiative recombination, diffusion, Auger recombination, etc. If the silicon ring waveguide dimension is less than 1 μm, nonradiative recombination dominates [5]. We can write the temporal evolution of the free carrier density as

$$\frac{\partial N}{\partial t} = \frac{c^2 \beta_2}{n_0^2 2\hbar \omega_L V_{FCA}^2}|u|^4 - \frac{N}{\tau_{car}}, \tag{2}$$

where N is the electron-hole pair density, $V_{FCA} = A_{FCA}L$ is the FCA volume and is defined as $A_{FCA}^2 = \frac{[\iint n(x,y)^2|\mathbf{E}|^2 dxdy]^3}{\iint_{Si} n(x,y)^6|\mathbf{E}|^6 dxdy}$ [5,19]. We simplify the free carrier lifetime τ_{car} as a fixed value, which does not change with the carrier density.

Similarly, we can introduce an equation to describe the temperature evolution in the silicon MRR. Heat generated inside the resonator comes from absorption—linear absorption, TPA, and FCA. Thermal energy in the waveguide diffuses to the surroundings mainly through heat conduction, thus we use the thermal decay time τ_{th} to describe the temperature evolution [5,19,20]

$$\frac{\partial \Delta T}{\partial t} = \frac{|u|^2}{\rho_{Si}c_{Si}V_{eff}}\left(\frac{\alpha_{abs}c}{n_0} + \frac{c^2 \beta_2 |u|^2}{n_0^2 V_{TPA}} + \frac{\sigma_{FCA}Nc}{n_0}\right) - \frac{\Delta T}{\tau_{th}}, \tag{3}$$

where ρ_{Si} and c_{Si} are the density and the constant-pressure specific heat capacity of silicon, respectively. $V_{eff} = A_{eff}L$ is the effective volume of the silicon waveguide.

The nonlinear system has three specific time-dependant parameters: photon lifetime (τ_{ph}), carrier lifetime (τ_{car}), and thermal decay time (τ_{th}). Photon lifetime is the average time that a photon can exist within the ring, which is determined by the total loss of the ring (including coupling loss) or equivalently, the cavity quality factor Q. Free carrier lifetime is mainly affected by the state of the silicon-silica interfaces. It is reported that the free carrier lifetime of an etchless silicon-on-insulator waveguide is one order of magnitude larger than that of the etched waveguide of the similar size [4,21]. Thermal decay time is mainly determined by the heat conduction rate, which is controlled by the material property and geometry. One reported experiment has shown that the thermal energy decay time can be engineered by etching trenches around the microring [4].

In this paper, we take a ridge waveguide with 220 nm height, 500 nm width, and 100 nm slab height as an example. Such ring resonator includes only one ring and one coupling waveguide, and the radius of the ring is 50 μm. The minimum linear loss reported is about 0.7 dB/cm for strip waveguide, while the linear loss of shallow-etched rib waveguide is less than 0.2 dB/cm by IMEC using optical lithography [22]. Thus, we use 0.7 dB/cm (0.16 cm^{-1}) as the loss of our ridge ring waveguide. Only critical coupling condition is considered in the numerical analysis. At this case, the photon lifetime calculated is 0.27ns [$\tau_{ph} = n_0/(c\alpha)$]. The values of parameters used in the calculation are listed in Table I.

TABLE I. Parameter values used in the calculation.

Parameter	Value	Unit	Source
n_0	2.588	–	FimmWave
α_{ring}	0.16	cm^{-1}	–
τ_{ph}	0.27	ns	calculated
η_{lin}	0.4	–	[2,19]
R	50	μm	–
n_2	4.5×10^{-18}	m^2/W	[23,24]
β_2	0.75×10^{-11}	m/W	[23,24]
σ_{FCA}	14.5×10^{-22}	m^2	[23,24]
A_{eff}	0.204×10^{-12}	m^2	FimmWave
A_{TPA}	0.1289×10^{-12}	m^2	Calculated
A_{FCA}	0.116×10^{-12}	m^2	Calculated
ρ_{Si}	2.329×10^6	g/m^3	[25]
c_{Si}	0.713	J/(g K)	[25]
κ_θ	1.86×10^{-4}	K^{-1}	[26]

B. Normalized equations and linear stability analysis

It is difficult to use Eqs. (1)–(3) to numerically analyze the nonlinear dynamic process directly, due to the large orders of magnitude differences of the parameters (u, N, and ΔT). For example, in some cases, the carrier density N is 10^{34} larger than the ring energy $|u|^2$ in number. Thus, it is very difficult to obtain correct dynamic results with Runge-Kutta method. Besides, it is also difficult to calculate the eigenvalues with linear stability analysis method directly, because of the very large quantitative differences among the elements in the matrix. A useful way is to normalize these parameters to dimensionless ones, which are shown below [8–11].

$$\frac{\partial a}{\partial t} = \{i\delta - i[n_{\text{Kerr}}|a|^2 - (n + \sigma_{\text{FCD}}n^{0.8}) + T]$$
$$- [1 + \alpha_{\text{TPA}}|a|^2 + \gamma_{\text{FCA}}n]\}a + \sqrt{P} \quad (4)$$

$$\frac{\partial n}{\partial t} = |a|^4 - \frac{n}{\tau} \quad (5)$$

$$\frac{\partial T}{\partial t} = \xi_T|a|^2\left(\eta_{\text{lin}}\eta_c + 2\alpha_{\text{TPA}}|a|^2 + 2\gamma_{\text{FCA}}n\right) - \frac{T}{\tau_\theta}, \quad (6)$$

where the normalized time t is in unit of $1/\Gamma_0$ with $\Gamma_0 = c\alpha/(2n_0)$. $|a|^2 = |u|^2\sqrt{\sigma\beta}$ is the normalized energy in the ring; $P = K_{\text{in}}P_{\text{in}}$ is normalized input power where $K_{\text{in}} = \sqrt{\sigma\beta}\Gamma_c/\Gamma_0^2$; $n = \sigma N$ is the normalized carrier density; $\delta = (\omega_0 - \omega_L)/\Gamma_0$ is the normalized input light frequency detuning; $n_{\text{Kerr}} = \omega_L n_2 c/(\Gamma_0 n_0^2 V_{\text{Kerr}}\sqrt{\sigma\beta})$ is the Kerr nonlinearity; $\sigma \equiv \sigma_{r1}\omega_L/(n_0\Gamma_0)$ and $\sigma_{\text{FCD}} = \sigma_{r2}\omega_L/(\sigma^{0.8}n_0\Gamma_0)$ are related to FCD effect; $T = \omega_L\kappa_\theta\Delta T/(n_0\Gamma_0)$ is the normalized temperature change corresponding to TO effect; $\alpha_{\text{TPA}} = \beta_2 c^2/(2n_0^2\Gamma_0 V_{\text{TPA}}\sqrt{\sigma\beta})$ is the TPA coefficient; $\gamma_{\text{FCA}} = \sigma_{\text{FCA}}c/(2n_0\Gamma_0\sigma)$ is the FCA absorption coefficient; $\tau = \Gamma_0\tau_{\text{car}}$ is the normalized carrier lifetime; $\beta \equiv c^2\beta_2/(\Gamma_0 2\hbar\omega_L n_0^2 V_{\text{FCA}}^2)$; $\xi_T = \omega_L\kappa_\theta/(n_0\Gamma_0\rho_{\text{Si}}c_{\text{Si}}V_{\text{eff}}\sqrt{\sigma\beta})$; $\eta_{\text{lin}} = \alpha_{\text{abs}}/\alpha_{\text{ring}}$ is the proportion of the linear absorption; $\eta_c = 2\alpha_{\text{ring}}/\alpha$ represents if the ring is at critical coupling ($= 1$), under coupling (> 1) or over coupling (< 1); $\tau_\theta = \Gamma_0\tau_{\text{th}}$ is the normalized thermal decay time.

Equations (4)–(6) have steady-state solutions $a(t) = A$, $n(t) = N_0$, $T(t) = T_0$ by letting $\partial a/\partial t = 0$, $\partial n/\partial t = 0$ and $\partial T/\partial t = 0$.

$$N_0 = \tau E^2 \quad (7)$$

$$T_0 = \tau_\theta\xi_T E(\eta_{\text{lin}}\eta_c + 2\alpha_{\text{TPA}}E + 2\gamma_{\text{FCA}}\tau E^2) \quad (8)$$

$$P = E\{[-\delta + n_{\text{Kerr}}E - (\tau E^2 + \sigma_{\text{FCD}}\tau^{0.8}E^{1.6}) + T_0]^2$$
$$+ [1 + \alpha_{\text{TPA}}E + \gamma_{\text{FCA}}\tau E^2]^2\}, \quad (9)$$

where $E = |A|^2$ is the intracavity normalized dimensionless energy.

For the normalized dimensionless equations (4)–(6), we can directly analyze the nonlinear system dynamics by using linear stability analysis which is similar to Refs. [8–11]. The corresponding linear matrix is obtained by adding small perturbations to the stable results and substituting the updated parameters into the normalized differential equations with omitting higher-order terms. Letting $a(t) = A + \delta a$, $n(t) = N_0 + \delta n$, and $T = T_0 + \delta T$, the perturbation array

$\varepsilon \equiv (\delta a, \delta a^*, \delta n, \delta T)^T$ is found to obey the linear equation

$$d\varepsilon/dt = M\varepsilon \quad (10)$$

where the eigenmatrix M is a 4×4 matrix. All the elements in M are listed below.

$$M = \begin{pmatrix} M_{11} & M_{12} & M_{13} & M_{14} \\ M_{21} & M_{22} & M_{23} & M_{24} \\ M_{31} & M_{32} & M_{33} & M_{34} \\ M_{41} & M_{42} & M_{43} & M_{44} \end{pmatrix} \quad (11)$$

with $M_{11} = i\delta - i2n_{\text{Kerr}}|A|^2 + i(N_0 + \sigma_{\text{FCD}}N_0^{0.8}) - iT_0 - 1 - \gamma_{\text{FCA}}N_0 - 2\alpha_{\text{TPA}}|A|^2$, $M_{12} = -in_{\text{Kerr}}A^2 - \alpha_{\text{TPA}}A^2$, $M_{13} = iA(1 + 0.8\sigma_{\text{FCD}}N_0^{-0.2}) - \gamma_{\text{FCA}}A$, $M_{14} = -iA$, $M_{21} = M_{12}^*$, $M_{22} = M_{11}^*$, $M_{23} = M_{13}^*$, $M_{24} = M_{14}^*$, $M_{31} = 2|A|^2A^*$, $M_{32} = M_{31}^*$, $M_{33} = -1/\tau$, $M_{34} = 0$, $M_{41} = \xi_T(\eta_{\text{lin}}\eta_c + 4\alpha_{\text{TPA}}|A|^2 + 2\gamma_{\text{FCA}}N_0)A^*$, $M_{42} = M_{41}^*$, $M_{43} = 2\xi_T\gamma_{\text{FCA}}|A|^2$, $M_{44} = -1/\tau_\theta$.

Thus, we can use the eigenvalues of M to find the boundaries of both BI and SP. Note that all the figures plotted in the next section are based on these normalized equations. After calculation, we then convert some dimensionless parameters back to the real physical parameters to give an intuitive physical view.

III. ANALYSIS OF BISTABILITY AND SELF-PULSATION

The normalized dimensionless equations [Eqs. (4)–(6)], together with the linear stability analysis method [Eq. (10)], are used to study the boundaries of both BI and SP. The resulted matrix is a 4×4 matrix with four eigenvalues [Eq. (11)]. If the real parts of all the eigenvalues are negative, it is called a stable node. On the other hand, if any of them is positive, it is called an unstable node [27]. In order to illustrate the BI and the SP conditions clearly, we assume $\lambda_{r1} \geqslant \lambda_{r2} \geqslant \lambda_{r3} \geqslant \lambda_{r4}$ as the real parts of the four eigenvalues. If $\lambda_{r1} > 0 > \lambda_{r2} \geqslant \lambda_{r3} \geqslant \lambda_{r4}$, this point is in the BI region, while if more than one of them is larger than 0, this point is in the SP region. Actually, there may be two pairs of complex conjugate eigenvalues or more than one real positive eigenvalues. As a result, the system considering TO effect is much more complicated than that only focusing on Kerr nonlinearity [28–31] or TPA nonlinearity [8,9].

As the relationship between input power and the energy in the ring (we use ring energy for simplicity) is not simply linear, the boundaries of BI and SP with respect to input power are complicated. An example of the relationship is shown in Fig. 1, assuming $\tau_{\text{car}} = 10$ ns, $\tau_{\text{th}} = 100$ ns and input light wavelength detuning $\Delta\lambda = -3$ pm, where different colors represent different energy states in the ring. The boundaries of the colored curves are determined by the eigenvalues of the linear stability matrix. In some cases, one input power corresponds to more than one ring energy state, thus the output power is determined by the initial ring energy state. For example, if one input power corresponds to two possible stable states of the ring, the actual output power is determined by the initial ring energy before the input light is injected into the ring; while if one input power corresponds to one
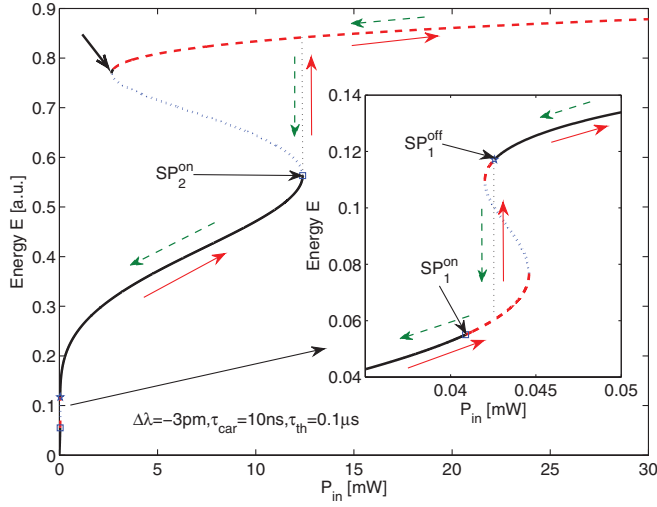
FIG. 1. (Color online) Ring energy E versus input power P_{in} in steady state. This figure is plotted by the steady-state relationship between normalized ring energy E and normalized input power P [see Eq. (9)]. Inset: zoom-in views when the input power is from 0.035 mW to 0.05 mW. Black solid curves: stable state; red dashed curves: self-pulsation state (SP); blue dotted curves: bistability state (BI). All the boundaries of these curves are determined by the linear stability analysis method [or the eigenvalues of matrix M, see Eq. (11)]. The red arrows represent input power changes from low to high, while the green ones represent the opposite direction. Two BI and three SP regions are found along with the ring energy, but only two SP regions are observed along with the input power.

FIG. 2. (Color online) Output power in through port versus input power. The inset is zoom-in view of the first SP region. The red curve describes the case where input power is increasing gradually, while the green dashed curve is for the opposite power changing direction. The blue dotted boxes represent the maximum possible output power ranges in SP regions. The irregular curves shown in SP regions are instantaneous values of output power at the same fixed time. All the values used in the figure are the same to those used in Fig. 1. Such curves are obtained by calculating Eqs. (4)–(6) with the Runge-Kutta method. At each input power, we read the output power and the ring state after 40 μs. The ring state was then used to be the initial state in calculating the next input power.

stable ring energy state and several unstable states, the output power usually chooses the stable one. As a result, with the increasing or decreasing of input power, some energy states are not obtained. In Fig. 1, only two SP regions are obtained. The two BI regions are within the two SP regions, thus we cannot see the hysteresis loop in the P_{out}-P_{in} plane (see Fig. 2). Furthermore, there is another stable energy state as the energy E is near 0.8, which is shown in short black curve in Fig. 1 (arrow). The range of such state is very narrow under this condition, but it will change with other parameters, such as input wavelength. Normally, it is difficult to reach this stable energy state with continuous change of input power. Some researchers have studied this condition by using short pulse laser and they observed the excitability [10,11,32]. Besides, in some cases changing input wavelength will reach this stable state, which will be shown in the following subsection.

A. Influence of input power and wavelength on bistability and self-pulsation

In this section, we analyze how the input light parameters (i.e., power and wavelength) affect the boundaries of BI and SP. It is convenient to use the steady-state solutions to show the relationship between the normalized refractive index change Δn and normalized ring energy E [Eqs. (7)–(9)], which is derived as follows:

$$\Delta n = n_{\text{Kerr}}E - (\tau E^2 + \sigma_{\text{FCD}}\tau^{0.8}E^{1.6}) + \tau_\theta \xi_T E(\eta_{\text{lin}}\eta_c + 2\alpha_{\text{TPA}}E + 2\gamma_{\text{FCA}}\tau E^2), \quad (12)$$

where the first term on the right-hand side is the Kerr effect, the second term within the bracket is the FCD effect, and the last one is the TO effect. The FCD effect has two parts, which illustrate the different roles of free electrons and holes in the refractive index. The TO effect has three parts: linear absorption, TPA absorption, and FCA absorption. The FCD effect decreases the refractive index, while Kerr and TO effects increase it. The sign of Δn is changed especially by the energy E – when E is very low, say near 0, TPA and its induced effects are so low that only the Kerr and linear absorption are in roles; while increasing E may make it negative according to the ratio of carrier lifetime and thermal decay time; when increasing E further, the FCA-induced TO effect will have the major effect on Δn.

When the carrier lifetime and thermal decay time are fixed to be 10 ns and 100 ns, respectively, the dimensionless parameters in Eq. (12) are calculated as: $n_{\text{Kerr}} = 0.55$, $\sigma_{\text{FCD}} = 7.2$, $\xi_T = 0.074$, $\alpha_{\text{TPA}} = 0.11$, $\gamma_{\text{FCA}} = 0.20$, $\tau = 18.5$, and $\tau_\theta = 185$, thus $\Delta n = 0.55E - (18.5E^2 + 74E^{1.6}) + 5.5E + 3E^2 + 101E^3$. Actually, there is a range of E where $\Delta n < 0$, which means the resonant wavelength of this MRR is blue-shifted. Multi-BI and multi-SP are the results of the competition of FCD and TO effects. Such a phenomenon was not predicted and observed in the systems where only FCD effect and/or Kerr effect is considered.

To further explore the possible multi-BI and multi-SP phenomena, we consider a fixed structure where the carrier lifetime and thermal decay time are constants. The map of BI and SP boundaries in the plane of input power and wavelength
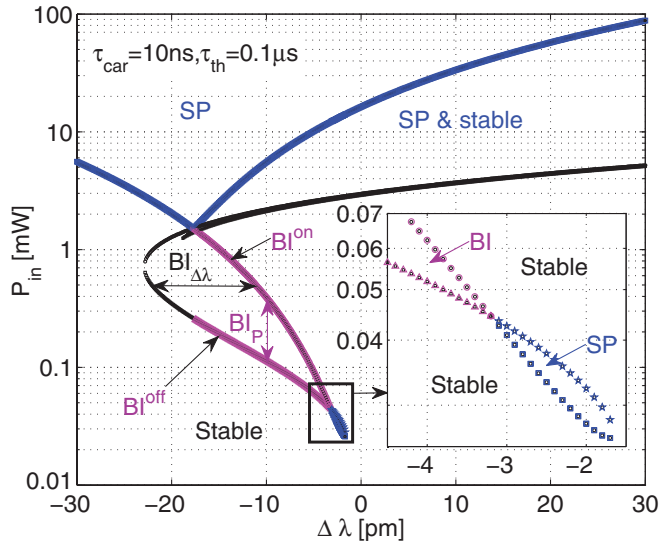
FIG. 3. (Color online) BI and SP boundaries in the map of input power (P_{in}) and wavelength detuning ($\Delta\lambda$). Inset: zoom-in details of the black box with input wavelength detuning from -1.5 pm to -4.5 pm. When the input power is from low to high, or the wavelength detuning is from blue to red, BI^{on} is the boundary of BI; for the opposite changing direction, BI^{off} is the boundary of BI. $\text{BI}_{\Delta\lambda}$ and BI_P represent the regions of BI in input wavelength and input power, respectively. All the black curves and markers are the boundaries of stable states, while some of them are also the boundaries of BI and/or SP.

FIG. 4. (Color online) Relative output power spectra at different input powers. Red solid curves represent the input wavelength from "blue side" to "red side" (which is from left to right in the figure), while the green dash-dot curves represent the opposite direction. $\tau_{\text{ph}} = 0.27$ ns, $\tau_{\text{car}} = 10$ ns, $\tau_{\text{th}} = 0.1$ μs.

detuning is very useful (see Fig. 3). A clear view of the map has shown that the minimum input power to stimulate SP is less than 20 μW. This results from the low loss of the MRR as well as the small effective area of the waveguide. The boundaries of BI are all blue-shifted from the linear resonant wavelength of MRR because of the predominant roles of FCD over other nonlinear effects. BI^{on} and BI^{off} are the boundaries of BI, which are defined according to the ring energy, $E(\text{BI}^{\text{on}}) < E(\text{BI}^{\text{off}})$, but $P(\text{BI}^{\text{on}}) > P(\text{BI}^{\text{off}})$ for input power. We should point out that the boundaries of BI in P_{in} and $\Delta\lambda$ are different where $\Delta\lambda < -17.5$ pm, and the main difference comes from BI^{off}. BI^{off} is on the upper stable branch of ring energy, and can only be obtained when the initial ring energy is high. When the input wavelength is from long to short, the energy state can reach the upper stable state branch, and thus it goes through the other boundary of BI. However, gradually changing input power is difficult to reach the upper branch of BI and thus only stable output power is observed in such input wavelength range. The mixed state "SP & stable" means that one input power corresponds to two different states: stable state and SP state. Normally, only stable output state is obtained, but a suitable input pulse may stimulate such output from stable to oscillation.

The output power versus input wavelength detuning at different input powers are shown in Fig. 4. Different wavelength sweeping directions have different output powers in the regions of BI. The main characteristic of BI is the hysteresis loop, which comes from the different initial ring energy states. When the input wavelength is swept from short to long, the initial ring energy is lower than $E(\text{BI}^{\text{on}})$ that BI^{on} is the first boundary of
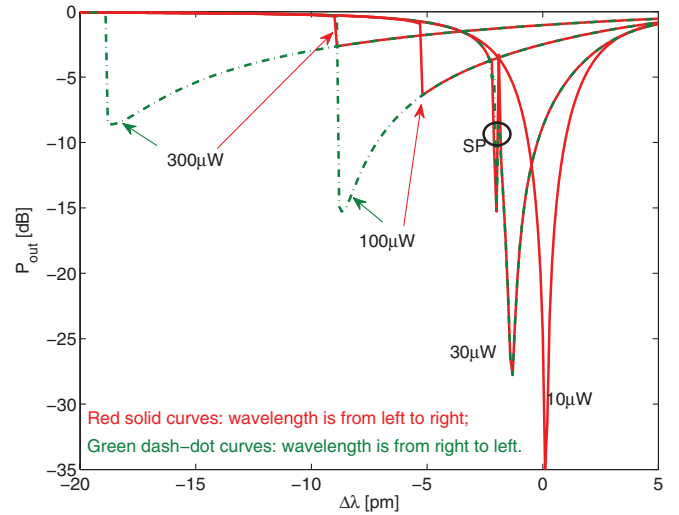
the ring energy, thus a sharp drop is obtained in output power. While if the input wavelength is swept from long to short such that the ring energy is different from previous situation, this results in a sharp change in the output power at BI^{off}. Furthermore, the SP is also observed in the optical spectrum when input power is 30 μW.

B. Characteristics of output light in different SP regions

From Fig. 3 it is also found that, if $\Delta\lambda$ is in the range of -3.1 pm to -1.7 pm, two input-power-dependent SP regions are observed. The major nonlinear effects in these two regions are different, so we further study how the output power oscillates in the time domain. Here Runge-Kutta method is directly used to calculate Eqs. (4)–(6), and the output parameters are then converted back to real physical parameters. The two input powers are 30 μW (we use SP_1 to define this SP region) and 20 mW (SP_2), respectively, with the same input wavelength detuning $\Delta\lambda = -2$ pm.

In SP_1, the output power has a periodic oscillation with high extinction ratio and nearly 50% duty ratio [Fig. 5(a)]. The limit cycle is obtained from the phase diagram of the output light field [Fig. 5(b) and the inset]. Fast Fourier transform (FFT) spectrum of the output power in the frequency domain shown in Fig. 5(c) indicates that the output light field has one major frequency near 3 MHz. This oscillation frequency is much lower than that of the case without considering TO effect, such as the previous simulation in Ref. [9]. To provide an insight into the process and the underlying physics, the refractive index change in the ring caused by Kerr effect, FCD effect, and TO effect were analyzed separately in the time domain as well, which are shown in Fig. 5(d). Kerr effect plays a negligible contribution to the refractive index change compared with other effects. FCD induced refractive index change, which is the embodiment of carrier density in the ring, holds a larger contribution than the TO effect does.
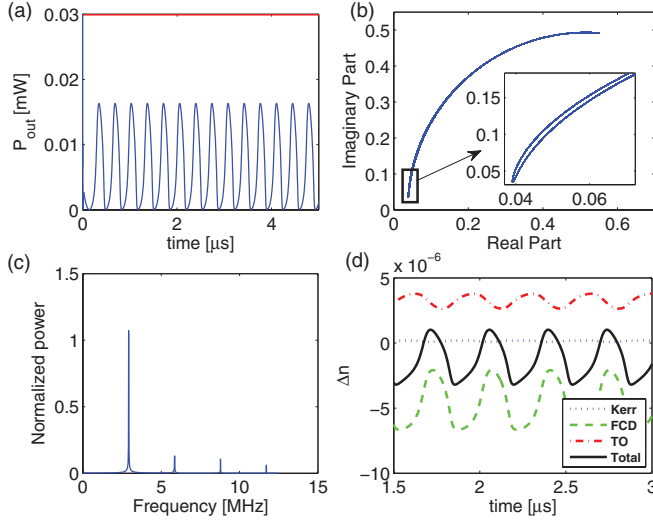
FIG. 5. (Color online) (a) Output power in time domain with input power 0.03 mW (within SP_1 region) and wavelength detuning -2 pm. (b) Phase diagram of the output light amplitude. The inset shows that it has only one limit cycle. (c) FFT spectrum of the output power. (d) Refractive index change in the ring waveguide caused by Kerr effect (blue dotted), FCD effect (green dash), and TO effect (red dash-dot), respectively. The sum result is shown in the black solid curve. $\tau_{ph} = 0.27$ ns, $\tau_{car} = 10$ ns, $\tau_{th} = 0.1$ μs.

In the SP_2 region, the SP characteristics are remarkably different from those in the SP_1 region. The output power is periodic [Fig. 6(a)] but without a single dominant frequency [Fig. 6(c)]. The phase diagram of the output light complex amplitude shows more complicated limit cycle as seen in Fig. 6(b). As shown in Fig. 6(d), the refractive index changes
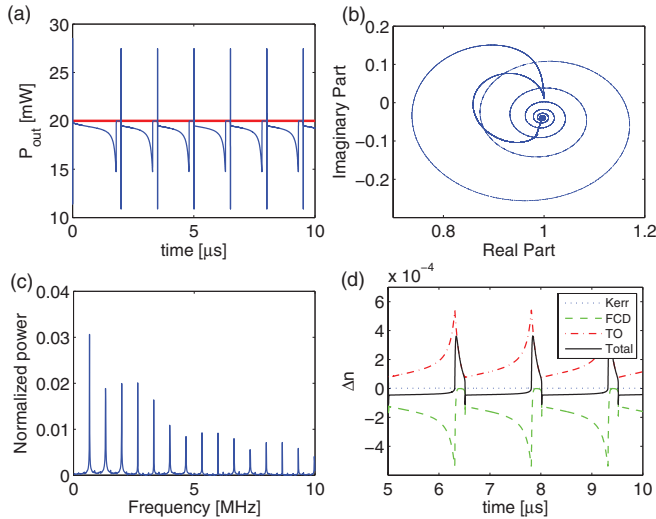
FIG. 6. (Color online) (a) Output power in time domain with input power 20 mW (red line, within SP_2 region) and wavelength detuning -2 pm. (b) Phase diagram of the output amplitude. (c) FFT spectrum of the output power. (d) Refractive index change in the ring waveguide caused by Kerr effect (blue dotted), FCD effect (green dash), and TO effect (red dash-dot), respectively. The sum result is shown in the black solid curve. $\tau_{ph} = 0.27$ ns, $\tau_{car} = 10$ ns, $\tau_{th} = 0.1$ μs.
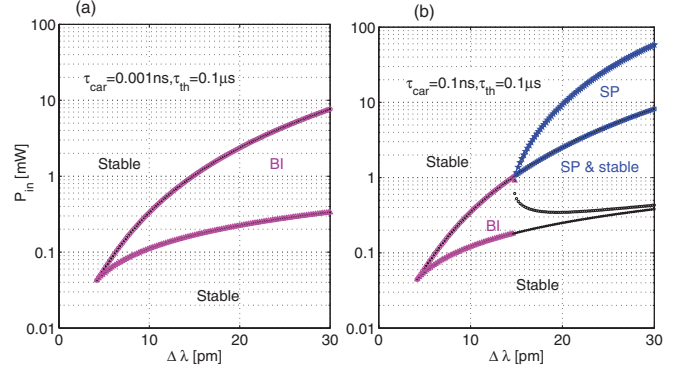
FIG. 7. (Color online) BI and SP boundaries in the map of input power (P_{in}) and wavelength detuning ($\Delta\lambda$). (a) Free carrier lifetime τ_{car} is fixed at 1 ps, which is much less than thermal decay time τ_{th} to simulate the limit value $\tau_{car}/\tau_{th} = 0$. (b) Free carrier lifetime is 0.1 ns ($\tau_{car}/\tau_{th} = 0.001$). SP is obtained at this case, which is shown within two blue curves. All the black curves and markers are the boundaries of stable states. $\tau_{ph} = 0.27$ ns.

smoothly in most time but with sharp rise and fall at the end of each oscillating cycle.

The sharp rise and fall of output power with time where the TO effect dominates comes from the fact that the ring energy state goes through the associated BI boundaries. For example, when the input power is very high, the ring energy increases from low to high and will undergo some BI states as seen in Fig. 1. The very high ring energy induces much more free carriers via TPA, leading to the increase of both $|\Delta n(\text{FCD})|$ and $\Delta n(\text{TO})$, and the power coupled into the ring will change according to the total refractive index. When E is not very large, $|\Delta n(\text{FCD})|$ is a slightly larger than $\Delta n(\text{TO})$. Therefore, the instantaneous resonant wavelength is blue-shifted slightly and is closer to the input wavelength, resulting in an increase of the coupling power into the ring. A quick increase of E then makes $\Delta n(\text{TO})$ increase quickly, then the instantaneous resonant wavelength is red-shifted and is far away from the input wavelength, resulting in a decrease of the coupling power into the ring. At this point, the first drop of E takes place, and the output power increases sharply. Then the energy E is very low where FCD is almost omitted, leaving only TO dominant. With the cooling of the ring waveguide, $\Delta n(\text{TO})$ is decreasing and the coupling power into the ring is increasing smoothly. When the ring energy is at the critical point, it would jump again, leading to another jump of output power. Because the temperature in the ring must be cooled down during one cycle, the total time in the cycle is much larger than the thermal decay time.

C. Influence of τ_{car}, τ_{th}, and τ_{ph} on multi-BI and multi-SP

First, we analyze how free carrier lifetime τ_{car} plays roles in BI and SP, by fixing the other two parameters constant. When the FCD effect is omitted, the TO effect is the main nonlinear effect. The refractive index change is positive and the ring resonant wavelength is red-shifted. The regions of BI and SP, if it has, are on the red side of the resonant wavelength. Two cases, $\tau_{car}/\tau_{th} = 10^{-5}$ and $\tau_{car}/\tau_{th} = 10^{-3}$, are analyzed through the map of BI and SP in the P_{in}- $\Delta\lambda$ plane (Fig. 7).
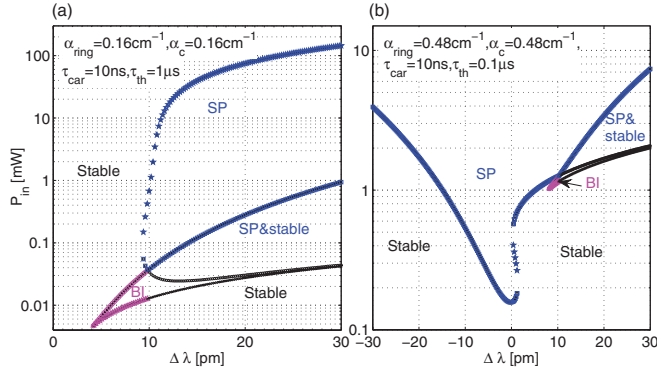
FIG. 8. (Color online) BI and SP boundaries in the map of input power (P_{in}) and wavelength detuning ($\Delta\lambda$). (a) Free carrier lifetime τ_{car} is 10 ns, thermal decay time τ_{th} is 1 μs. The ring linear loss is 0.16 cm^{-1} with $\tau_{ph} = 0.27$ ns. (b) Free carrier lifetime τ_{car} is 10 ns, thermal decay time τ_{th} is 0.1 μs. The ring linear loss is 0.48 cm^{-1} with $\tau_{ph} = 0.09$ ns.

The main feature is that the regions of BI and SP are all in the red-shifted wavelength range, which fits well with the above discussion. When the free carrier lifetime is enlarged, the region of SP is observed [Fig. 7(b)].

One necessary condition for SP in the silicon MRR is that both FCD and TO have similar functions on the refractive index change. With the increase of carrier lifetime, the range of SP enlarges, while the range of BI shrinks (due to the intersection of BI and SP). Enlarging the free carrier lifetime further will get a whole wavelength detuning range of SP, which can be understood from Fig. 3 as one example. The threshold input power of SP will reach its minimum value as well.

The thermal decay time τ_{th} can also be tailored, such as by etching trenches around the microring [4], or by controlling the cladding thickness or material. The influence of τ_{th} on BI and SP is inverse to that of τ_{car}, due to the fact that FCD and TO play opposite roles in the refractive index change Δn. One example of such case is shown in Fig. 8(a) by assuming $\tau_{th} = 1$ μs and $\tau_{car} = 10$ ns. Both BI and SP regions are in the red-shift range, which is similar to the case of Fig. 7(b).

With further increase of the free carrier lifetime (or decrease of the thermal decay time), FCD contributes more to Δn than TO, resulting in an overall blue-shift of BI. The threshold power of SP increases accordingly. The limit situation in this case is $\tau_{car}/\tau_{th} \to \infty$. This indicates that the TO effect is omitted, which was already analyzed by us [9]. Under this condition, the dynamic system is mainly determined by the photon lifetime and the free carrier lifetime. Similar BI and SP regions occur when other suitable parameter values are adopted.

Thirdly, we analyze how the photon lifetime τ_{ph} affects BI and SP. The photon lifetime is inversely proportional to the ring linear loss [$\tau_{ph} = n_0/(c\alpha)$]. The way to change τ_{ph} is to change the ring linear loss α of MRR, for example, to change the gap between the straight waveguide and the ring waveguide, or to change the roughness of the sidewall of MRR. It is well known that the quality factor Q of MRR is also inversely proportional to the ring loss. Thus, both τ_{ph} and Q are affected by the ring
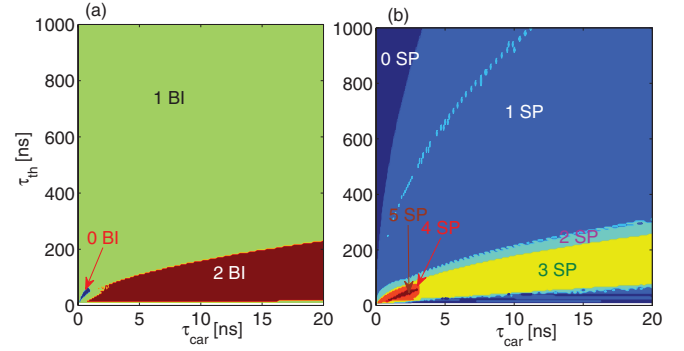
FIG. 9. (Color online) Maximum energy states number of BI (a) and SP (b) in the map of (τ_{car}, τ_{th}) with $\Delta\lambda$ from -20 pm to 20 pm and P_{in} from 0 to 1 W. The minimum steps of carrier lifetime τ_{car}, and thermal decay time τ_{th} are 0.05 ns and 5 ns, respectively. $\alpha_{ring} = \alpha_c = 0.16$ cm^{-1}, $\tau_{ph} = 0.27$ ns. The rough edges of the regions are due to the relative large steps of τ_{car}, τ_{th} and $\Delta\lambda$.

linear loss. The linear loss used is 0.16 cm^{-1} (0.7 dB/cm) in the simulation, resulting in a very high intrinsic quality factor (about 1 million), and photon lifetime of 0.27 ns. Such large quality factor reduces the threshold power of both BI and SP due to the high power enhancement effect of the MRR. Changing the photon lifetime would make the dynamic process among τ_{car}, τ_{th}, and τ_{ph} no more in balance, thus the regions of BI and SP change [Fig. 8(b)].

Finally, we give the statistical maximum numbers of ring energy states (BI and SP) in MRR with free carrier lifetime from 100 ps to 20 ns and thermal decay time from 10 ns to 1 μs by fixing the photon lifetime at 0.27 ns (Fig. 9). To obtain the maximum number of ring energy states at each (τ_{car}, τ_{th}), a range of input power and wavelength are used, i.e., the input power is from 0 to 1 W and the input wavelength detuning is from -20 pm to 20 pm. The region where two BI states exist is referred to as the "co-work" region, which means both FCD and TO have impacts on the refractive index. In the co-work region, the maximum numbers of SP states in the MRR are observed from 2 to 5. The case of four and five SP states show that these three time constants (τ_{car}, τ_{th}, and τ_{ph}) all take effect. Besides, it is not a linear relationship between τ_{car} and τ_{th} at each energy state boundary.

IV. CONCLUSION

In this work we have studied the behaviors and boundaries for both bistability and self-pulsation in silicon MRRs with coupled mode theory and linear stability analysis, taking into account of thermo-optical effect and other nonlinear effects. Importantly, with normalizing the coupled mode equations to dimensionless ones and with the eigenvalues of the stability matrix, we have found input-power-dependent multi-BI and multi-SP regions at certain input wavelength, free carrier lifetime and thermal decay time. We have further analyzed the roles of carrier lifetime, thermal decay time, and photon lifetime on the BI and SP, and found that the boundaries and the region numbers of BI and SP change with these time constants. The threshold power of the associated nonlinear phenomena is only several tens of μW in high Q silicon MRRs, which is, on the one hand, beneficial for the potential applications

in all-optical nonlinear devices, yet on the other hand, may be detrimental for the stable operation of linear optical devices. Moreover, such multi-BI and multi-SP phenomena may broaden the all-optical application of silicon MRRs.

[1] L. W. Luo, G. S. Wiederhecker, J. Cardenas, C. Poitras, and M. Lipson, Opt. Express **19**, 6284 (2011).

[2] G. Priem, P. Dumon, W. Bogaerts, D. V. Thourhout, G. Morthier, and R. Baets, Opt. Express **13**, 9623 (2005).

[3] W. H. P. Pernice, M. Li, and H. X. Tang, Opt. Express **18**, 18438 (2010).

[4] L. W. Luo, G. S. Wiederhecker, K. Preston, and M. Lipson, Opt. Lett. **37**, 590 (2012).

[5] T. J. Johnson, M. Borselli, and O. Painter, Opt. Express **14**, 817 (2006).

[6] M. Notomi, A. Shinya, S. Mitsugi, G. Kira, E. Kuramochi, and T. Tanabe, Opt. Express **13**, 2678 (2005).

[7] K. Ikeda and O. Akimoto, Phys. Rev. Lett. **48**, 617 (1982).

[8] S. Malaguti, G. Bellanca, A. de Rossi, S. Combrié, and S. Trillo, Phys. Rev. A **83**, 051802(R) (2011).

[9] S. Chen, L. Zhang, Y. Fei, and T. Cao, Opt. Express **20**, 7454 (2012).

[10] T. VanVaerenbergh, M. Fiers, P. Mechet, T. Spuesens, P. Kumar, G. Morthier, B. Schrauwen, J. Dambre, and P. Bienstman, Opt. Express **20**, 20292 (2012).

[11] T. VanVaerenbergh, M. Fiers, J. Dambre, and P. Bienstman, Phys. Rev. A **86**, 063808 (2012).

[12] R. Dekker, N. Usechak, M. Forst, and A. Driessen, J. Phys. D: Appl. Phys. **40**, R249 (2007).

[13] J. Leuthold, C. Koos, and W. Freude, Nature Photon. **4**, 535 (2010).

[14] H. A. Haus, M. A. Popovic, M. R. Watts, C. Manolatou, B. E. Little, and S. T. Chu, in *Optical Microcavities*, Vol. 5, edited by K. Vahala, 1st ed. (World Scientific, Singapore, 2004), Ch. 1, pp. 1–38.

[15] A. de Rossi, M. Lauritano, S. Combrié, Q. V. Tran, and C. Husko, Phys. Rev. A **79**, 043818 (2009).

[16] V. Van, T. A. Ibrahim, P. P. Absil, F. G. Johnson, R. Grover, and P.-T. Ho, IEEE J. Sel. Top. Quantum Electron. **8**, 705 (2002).

[17] B. E. Little, S. T. Chu, H. A. Haus, J. Foresi, and J.-P. Laine, J. Lightwave Technol. **15**, 998 (1997).

[18] R. A. Soref and B. R. Bennett, IEEE J. Quant. Electron. **QE-23**, 123 (1987).

[19] P. E. Barclay, K. Srinivasan, and O. Painter, Opt. Express **13**, 801 (2005).

[20] Q. Xu and M. Lipson, Opt. Lett. **31**, 341 (2006).

[21] V. R. Almeida, C. A. Barrios, R. R. Panepucci, and M. Lipson, Nature (London) **431**, 1081 (2004).

[22] S. K. Selvaraja, G. Murdoch, A. Milenin, C. Delvaux, P. Ong, S. Pathak, D. Vermeulen, G. Sterckx, G. Winroth, P. Verheyen, G. Lepage, W. Bogaerts, R. Baets, J. Van Campenhout, and P. Absil, *17th Opto-Electronics and Communications Conference, Abstracts* (IEEE, Busan, Korea, 2012), pp. 15–16.

[23] Q. lin, O. J. Painter, and G. P. Agrawal, Opt. Express **15**, 16604 (2007).

[24] H. K. Tsang and Y. Liu, Semicond. Sci. Technol. **23**, 064007 (2008).

[25] S. M. Sze and K. K. Ng, *Physics of Semiconductor Devices*, 3rd ed. (Wiley, New York, 2006).

[26] G. Cocorullo and I. Rendina, Electron. Lett. **28**, 83 (1992).

[27] M. Tabor, *Chaos and Integrability in Nonlinear Dynamics: An Introduction* (Wiley, New York, 1989).

[28] A. Parini, G. Bellanca, S. Trillo, M. Conforti, A. Locatelli, and C. D. Angelis, J. Opt. Soc. Am. B **24**, 2229 (2007).

[29] B. Maes, M. Fiers, and P. Bienstman, Phys. Rev. A **80**, 033805 (2009).

[30] A. Armaroli, S. Malaguti, G. Bellanca, S. Trillo, A. de Rossi, and S. Combrié, Phys. Rev. A **84**, 053816 (2011).

[31] Y. Dumeige and P. Féron, Phys. Rev. A **84**, 043847 (2011).

[32] M. Brunstein, A. M. Yacomotti, I. Sagnes, F. Raineri, L. Bigot, and A. Levenson, Phys. Rev. A **85**, 031803(R) (2012).